Structural analysis of HZO thin film and electrode using X-ray diffraction

Elliot Winsnes

Thesis submitted for the degree of Bachelor of Science
Project duration: 2 months

Supervised by: Jesper Wallentin, Megan Hill, and Huaiyu Chen

Abstract

Since its discovery in 2011, the ferroelectricity of thin films based on HfO_2 has been studied intensively. In particular, thin films with a 1:1 ratio of HfO_2 and ZrO_2 (HZO) has been of great interest. The ferroelectricity arises from a non-centrosymmetric orthorhombic (o) phase of HZO whose prevalence is dependent on the processing conditions. One of these processing conditions is the annealing temperature. While higher temperatures has been shown to better crystallize the o-phase, such temperatures will hinder device implementation since the interface with a semiconductor will be damaged. The texturing of TiN top electrodes has also been shown to impact the crystallization of HZO, with a (111) texturing resulting in a larger o-phase fraction. In this paper, the nanoprobe X-ray diffraction imaging of the NanoMAX beamline at the synchrotron radiation facility MAX IV, Lund, Sweden, is utilized in order to disclose any regional phenomena in a $370^{\circ}C$ thermally annealed sample consisting of a TiN (10 nm) bottom electrode and a TiN/Au (10 nm/200 nm) top electrode with HZO (12 nm) sandwiched in between. This provides new insight into the uniformity of the sample, not made possible by typical XRD measurements which are on the mm-μm scale which does not allow for precise imaging.

The results show peaks arising from the o-phase in all of the diffraction spectra of the different points in the sample, indicating that the sample preparation was successful in crystallizing all of the sample in the o-phase. The spatial investigation of the sample shows peak-shifting in a region, multiple potential contributions to this are discussed. Grain size analysis from the Scherrer equation shows a minimum grain size of $\tau \sim 19$ nm, which is larger than the film thickness itself. This behavior can not be explained but has been seen observed previously. For a real investigation of the grain size, other methods would have to be utilized. Finally, the TiN electrode peaks in the XRD spectrum exhibit (111) texturing, ideal for the crystallization in the o-phase. The work displays that HZO thin films can be studied using an X-ray nanoprobe, and a more optimized sample could be investigated further using the same method. This would provide deeper insight into the uniformity of HZO thin films.

Contents

1 Introduction

Over the last decade, the study of $Hf_{0.5}Zr_{0.5}O_2$ (HZO) for its ferroelectric (FE) properties has been of great interest to the semiconductor industry. FE materials have many applications, in particular in ferroelectric-random-access-memory (FRAM). There are several advantages of FRAM compared to conventional flash memory, including low power operation (1.5 V vs >10 V), faster write speed ($\sim$ 50 ns vs $\sim$ 1 ms) and an "infinite" number of writes (10^{15} vs 10^5) [24]. Commercial FRAM operating at 1.5 V has been manufactured using 70 nm thick $Pb(Zr,Ti)O_3$ (PZT) films. A huge problem regarding PZT are the environmental and regulatory issues that exist due to the use of toxic material containing Pb [28]. PZT also hinders the scaling down of devices it is implemented in, and as devices currently implementing PZT are getting smaller, alternative FE materials would thus have to be utilized. PZT has a band gap of 3-4 eV, which in implementation in transistors would lead to a high leakage current if it is scaled down further [24]. Further down-scaling of capacitors would also eventually require 3D geometry, instead of planar capacitors, which would make the atomic layer deposition (ALD) method difficult due to the large and easily evaporated Pb atoms [24]. Oxygen vacancies, which are a concern for the reliability, are also prevalent in PZT due to the relatively weak binding with the oxygen [28].

With all these issues with traditional perovskite ferroelectrics, an alternative ferroelectric material has been sought after. The first report on the ferroelectricity of thin 10 nm HfO_2 based films was published in 2011 and kickstarted the interest in using it as a FE material [7]. HfO_2 based thin films, where HZO is the most prevalent, can overcome the issues with conventional PZT. HfO_2 based materials had previously been studied for their high dielectric constant in the tetragonal (t)- and cubic (c)-phase, which only appear at temperatures above 1750°C and 2700°C respectively, with the monoclinic (m)-phase being stable at room temperature [35, 12]. Since the dielectric phases are metastable at room temperature, Hf was doped with Si in order to crystallize in the t- or c-phase. It was this doping of HfO_2 thin films with SiO_2 that first lead to the discovery of ferroelectricity in such films. First discovered in 2007 at the German dynamic random access memory (DRAM) manufacturer Qimonda, experiments continued until 2011 when the first report was released by Böscke et al. [24].

The FE behaviour is believed to arise from the non-centrosymmetric orthorhombic (o), space group $Pbc2_1$, phase of HZO. While pure HfO_2 exhibits a centrosymmetric m-phase and pure ZrO_2 is of centrosymmetric t-phase in a thin film, the $Hf_{1-x}Zr_xO_2$ mixed oxide has been shown to contain the non-centrosymmetric o-phase [30]. The FE behaviour is non-existent for $x = 0$, reaches its maximum when the composition contains equal amount HfO_2 and ZrO_2 and then becomes anti-ferroelectric as x approaches 1 [30]. The o-phase of doped HfO_2 is believed to arise from four main factors during the production: the compound fractions and annealing of the sample, the stress induced in the film, the interface with the electrodes, and the film thickness [24]. XRD provides the ability for the study of the crystal structure of HZO, which must contain the o-phase for FE switching. Purely studying the electric properties does not give any information of the underlying phenomena. From the XRD data it can thus be shown if the production method for the sample was successful and indeed resulted in a prevalent o-phase, if the other phases dominate, or if the sample is amorphous.

In this paper, a sample annealed at 370°C consisting of a TiN bottom electrode and a TiN/Au top electrode, with HZO sandwiched in between, will be studied (fig. 1). This is a lower temperature than many other studies of HZO, while still being able to crystallize HZO in the o-phase. It is of high importance to study how well it does crystallize in this phase as lower an-
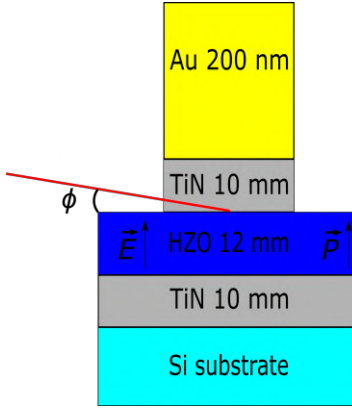
Figure 1: Illustration of the thermally annealed sample. Note that the Au is not to scale. The goniometer angle ϕ is shown, as well as the polarization $\vec{P}$ from the the applied electric field $\vec{E}$ as a result of the dipole alignment illustrated in fig. 4.

nealing temperatures would allow for integration with semiconductors that would be damaged by higher temperatures [32]. Utilizing X-ray diffraction (XRD) at the NanoMAX beamline at the MAX IV synchrotron radiation facility in Lund, Sweden, the nano focused X-ray beam could provide new insight into the o-phase responsible for ferroelectricity. In particular, the imaging will be utilized to study possible regional changes of the o-phase in the sample, which is not possible in typical XRD measurements due to the large beam focus. This thesis as such demonstrates that HZO suits itself to be studied using a nanoprobe, and how this can de done. Specifically, potential regional alterations to the high-intensity o(111) peak will be observed. The Scherrer equation (6) will also be utilized to analyze the grain size of the o-phase. The imaging will allow for separation of the diffraction spectrum not off the top electrode (off-contact) and the diffraction spectrum off the top electrode (on-contact), which could help to discern features that are buried by the large intensity of the Au top electrode. In addition to this, the TiN texturing, which has been shown to impact the phase composition of HZO films, will also be studied. This is done by observing peaks arising from diffraction off the TiN in the diffraction spectrum. In particular, (111) texturing has been shown to lead to a higher o-phase fraction, and the TiN peaks being predominantly from the (111) plane would thus demonstrate that the deposition of the TiN with the desired texturing was successful [4].

2 Theory

2.1 The solid structure of HZO

The following section is based on Hofmann [15]. The atomic structure of a crystallized solid can be described using the concept of the lattice. Using that the solid consists of a regularly spaced ions, the "Bravais lattice" is defined through the vector

$$\vec{R} = n_1\vec{a}_1 + n_2\vec{a}_2 + n_3\vec{a}_3 \tag{1}$$

where n_i are integers and $\vec{a}_i$ are lattice vectors. Every point in the lattice can be reached by $\vec{R}$ and in every point in the Bravais lattice there is what is referred to as a "basis". This basis can consist of one, but also several ions or molecules. A primitive unit cell is the smallest repeating unit within the crystal structure of the solid such that when translated through the lattice constants, it generates the entire Bravais lattice. In 3D there are 14 different Bravais lattices, which can be grouped into 7 different crystal classes: cubic, tetragonal, hexagonal,

2

orthorhombic, monoclinic, triclinic, and trigonal. The crystal classes can be of four different types: primitive, body-centered, face-centered, and base-centered. All crystal structures can be primitive, but not all can appear in the other types, which all together gives the 14 different Bravais lattices. These different crystal structures can be grouped into different space groups, of which there are are 230 in total. For each crystal structure, there as such exists several ways the ions can orient themselves such that different properties emerge, e.g the same crystal structure can both be centrosymmetric and non-centrosymmetric depending on its space group.

The Fourier transform of the Bravais lattice, $\vec{R}$ is called the reciprocal lattice, $\vec{K}$:

$$\vec{K} = h\vec{b_1} + k\vec{b_2} + l\vec{b_3}. \tag{2}$$

where h, k, and l are integers and $\vec{b_i}$ the reciprocal lattice vectors. As $\vec{K}$ is the Fourier transform of $\vec{R}$, it has the property that $\vec{R} \cdot \vec{K} = 2\pi n$, where n is an integer. The reciprocal lattice allows for the characterisation of the lattice planes through the use of Miller indices. The lattice planes are planes in the Bravais lattice intersecting the three axes at an in integer multiple of $|\vec{a_i}|$ (including at ∞). Taking the inverse of these integers ($\frac{1}{n_1}$, $\frac{1}{n_2}$, $\frac{1}{n_3}$), and multiplying with a factor to make them all integers gives (h, k, l) from the reciprocal lattice (2). These three integers are referred to as the Miller indices and are used to describe the lattice planes. All crystallite solids consists of such lattice planes.

When deposited on the substrate, HfO_2 is amorphous and crystallizes through annealing [23]. There are three common crystal phases of HfO_2: m-phase at room temperature, t-phase at temperatures exceeding 2050 K, and a cubic phase for temperatures above 2803 K [39]. In thin films, the surface interface is large compared to the bulk, which results in large surface energy. In a HfO_2 thin film, this results in crystallization in the t-phase at lower temperatures normally reserved for the m-phase. However, while HfO_2 nucleates in the t-phase, it tends to undergo a martensitic transition to the m-phase. A martensitic transition is a transition where groups of ions reorient in the lattice, such that the relative positions between atoms in that group remains the same. Thin ZrO_2 films tend to form in the t-phase when deposited. Müller et al. [30] demonstrated that for different mixtures of HfO_2 and ZrO_2, different crystal classes tend to dominate. In Hf-rich samples, mostly centrosymmetric m-phase was exhibited from the sample, while samples rich in Zr predominantly exhibited centrosymmetric t-phase. When mixed however, a non-centrosymmetric o-phase that could not be attributed to pure HfO_2 or ZrO_2 was observed.

The device studied in this work used HZO grown on Si/TiN with top electrodes of TiN/Au, as seen in fig. 1. The m space group, $P2_1/c$, of pure HfO_2 has estimated lattice constants $|\vec{a_1}| = 5.14$ Å, $|\vec{a_2}| = 5.07$ Å, and $|\vec{a_3}| = 5.29$ Å with an angle $99.56°$ between $\vec{a_2}$ and $\vec{a_3}$ [18, 30]. The t space group, $P4_2/nmc$, of ZrO_2 has estimated lattice constants $|\vec{a_1}| = |\vec{a_2}| = 3.59$ Å, and $|\vec{a_3}| = 5.17$ Å [30]. When HfO_2 and ZrO_2 crystallize in a space group $Pca2_1$ o-phase, they display very similar properties. HfO_2 has estimated lattice constants $|\vec{a_1}| = 5.22$ Å, $|\vec{a_2}| = 5.00$ Å, and $|\vec{a_3}| = 5.03$ Å, while ZrO_2 has estimated lattice constants $|\vec{a_1}| = 5.28$, $|\vec{a_2}| = 5.07$, and $|\vec{a_3}| = 5.10$ Å [18]. It is the similarity of the physical and chemical properties of Hf and Zr that allow for a compound with a 1:1 ratio of these two. All these phases are displayed in fig. 2. $Pbc2_1$ o-phase HZO has been measured to have the intermediate lattice constants $|\vec{a_1}| = 5.24$ Å, $|\vec{a_2}| = 5.01$ Å, and $|\vec{a_3}| = 5.05$ Å [30]. TiN was used as top and bottom electrode, see fig 1. It has a cubic structure with approximately $|\vec{a_i}| = 4.238$ Å [36]. The (002) and (111) lattice planes are shown in fig. 3. Depending on the texturing of the electrodes, different lattice planes will scatter more or less X-rays, affecting the intensities in
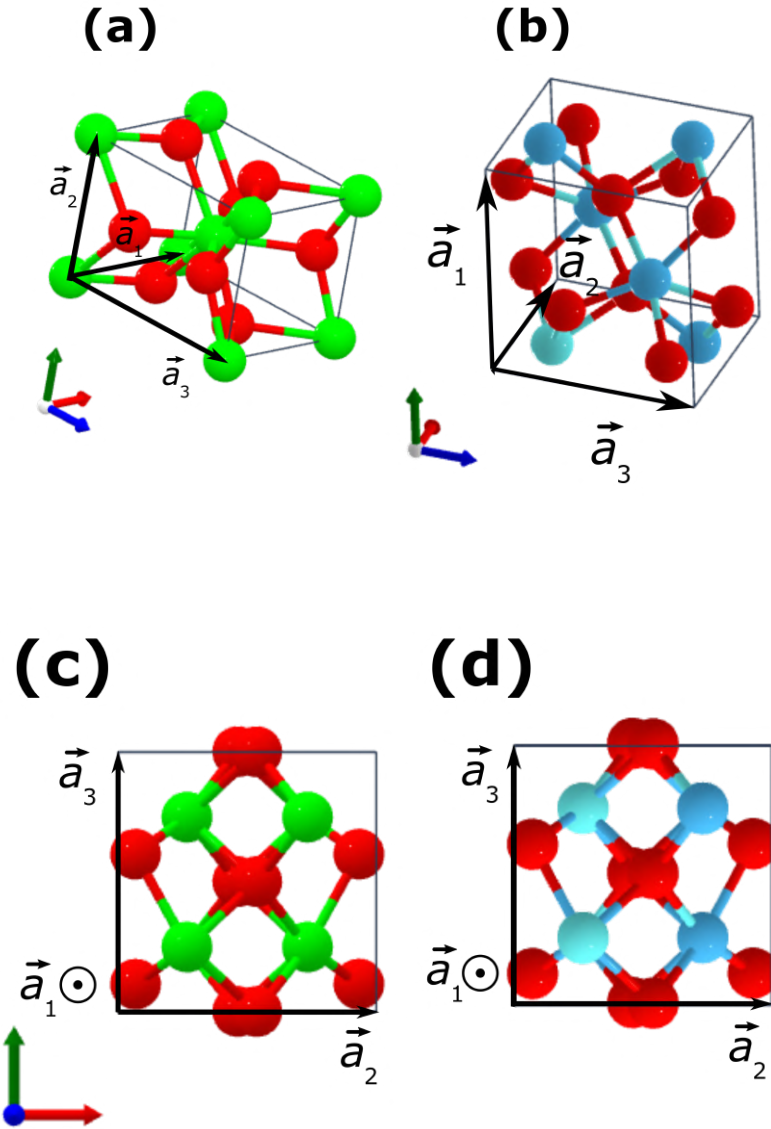
Figure 2: **(a)** The tetragonal $P4_2/nmc$ space group unit cell of ZrO_2. **(b)** The monoclinic $P2_1c$ space group of HfO_2. **(c)** The non-centrosymmetric orthorhombic phase ($Pca2_1$), space group of ZrO_2. **(d)** The non-centrosymmetric orthorhombic phase ($Pca2_1$), space group of HfO_2. Note that these $Pca2_1$ o-phases are not the same as the $Pbc2_1$ space group of o-phase HZO. All images taken from Material Project [18]
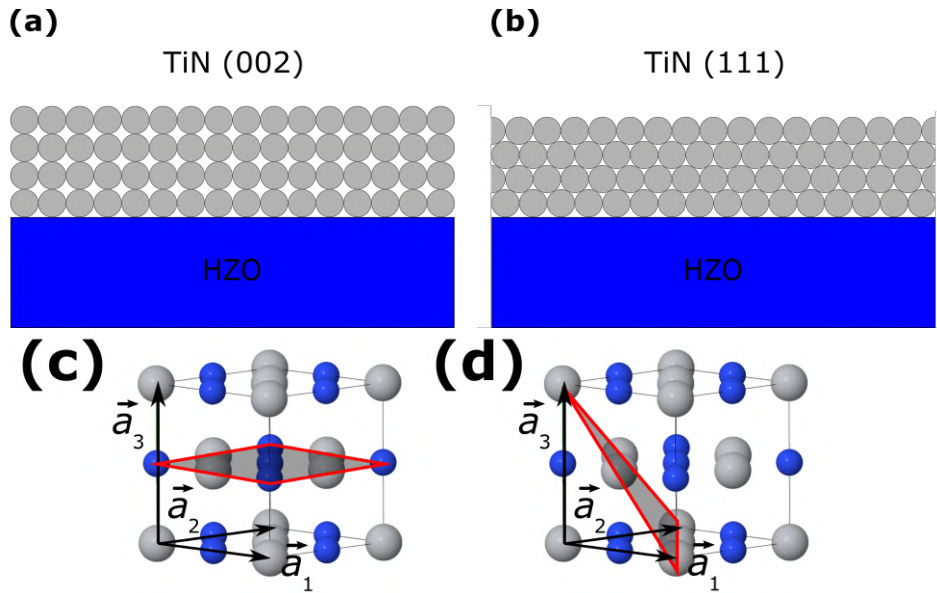
Figure 3: **(a)** Illustration of a TiN electrode with (002) texturing. Note that the illustration depicts a perfect crystal that would result in a perfect Bragg peak. In reality the planes are not perfectly aligned as depicted, and the X-rays will thus diffract at slightly different angles. **(b)** TiN electrode with (111) texturing. Note that this also depicts a perfect crystal. **(c)** TiN cubic unit cell with the (002) plane marked. **(d)** TiN cubic unit cell with the (111) plane marked. Images taken from Springer and modified [36].

the diffraction spectrum. The Ti atoms has an FCC structure and between two Ti atoms there is an N atom, see fig. 3. Au is also cubic with a lattice constant of approximately $|\vec{a}_i| = 4.17$ Å [18].

2.2 Ferroelectricity

Ferroelectricity is the spontaneous polarization of a material without an applied electric field. This means that there is a separation of positive and negative charge in the lattice. In a crystallite solid, electropositive atoms tend to transfer their electron to a neighbouring electronegative atom [15]. If there is a shifting of a sublattice, consisting of ions, with regards to the main lattice, consisting of oppositely charged ions, a permanent electric dipole resulting in polarization is created.

The ferroelectricity of doped HfO_2 thin films had not been predicted before its discovery and eventual publication in 2011 by Böscke et al. [7], where they doped with SiO_2. They investigated the sample with grazing incidence XRD, which is more surface sensitive than XRD. What they found agreed with diffraction measurements for Mg stabilized ZrO_2, which contained peaks arising from the rare non-centrosymmetric $Pbc2_1$ space group [27]. Since the doped Hf also showed FE behaviour, it was proposed that the ferroelectricity arose from the $Pbc2_1$ o-phase [7]. The same year, first report on FE HZO was released, where Müller et al. [29] showed that the same o-phase could be reached but at a lower thermal budget than for SiO_2.

In the traditional FE perovskite $PbTiO_3$, the ferroelectricity is a result of a displacement of the central Ti^{4+} with regards to the four O^{2-} surrounding it. This happens because of a combination of the atomic orbitals of the Pb and O hybridizing, and covalent bonds between
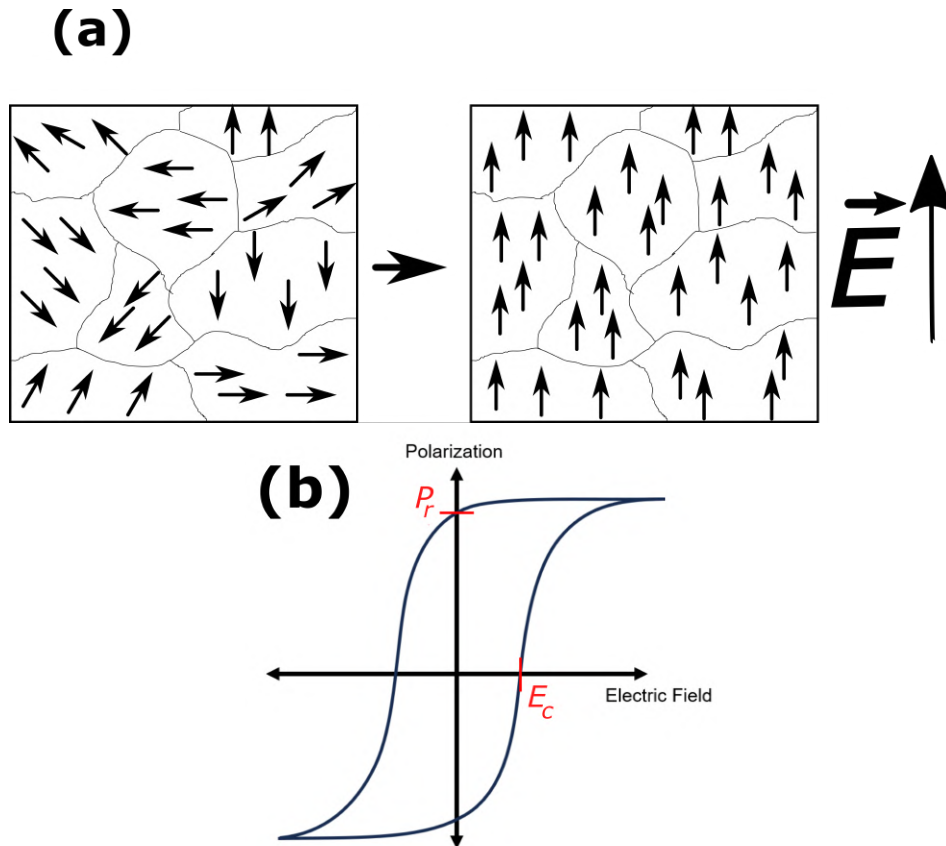
Figure 4: **(a)** Illustration of the FE domains aligning with the external electric field. Arrows show the direction of the dipole moments in the domains. **(b)** The characteristic hysteresis loop of a ferroelectric. P_r is the remanent polarisation and E_c the coercive electric field.

the ions, resulting in strain that stabilizes in the FE t-phase [10]. The bonding of the atoms in HZO differs from this in that it seems to have both ionic and covalent bonding [40]. The influence of the covalent bonds has not been known, but recent computations by Yuan et al. [40] show that the ferroelectricity is not dependent on the covalent bonds. While the reasons are complex and will not be thoroughly discussed here, a short summary is as follows. The number of anions to which a cation bonds is called the cation coordination number (CCN). This number is proportional to the ratio between the cation and anion radii. The CCN number is 8 for the t-phase and 7 for the m- and o-phase. If the radii ratio favors a CCN of exatly 7, no ferroelectricity is achieved since the m-phase is favoured. However, close to a CCN of 6 or 8, the barrier required to switch to the o-phase is lowered. This is how ferroelectricity is achieved in HZO. The atomic radii ratio of Zr/O is larger than that of Hf/O, leading to a CCN close to 8 which significantly lowers the switching barrier to the o-phase and suppresses the m-phase.

The result is the non-centrosymmetric o-phase where the Hf^{4+}/Zr^{4+} and O^{2-}, that make up the lattice, have reorganized in a non-uniform way. The O^{2-} ions have shifted with regards to the Hf^{4+}/Zr^{4+}, resulting in a non-centrosymmetry. Different domains of the material are polarized in different directions, such that the material does not display any net polarization. An external electric field can align the dipoles in the same direction, such that when the electric field is removed the material exhibits a remanent polarization, P_r, as illustrated in fig. 4(a). Through an external electric field, the remanent polarization direction of the

material can thus also be controlled. The field required in order to make the net polarization zero is called the coercive field, E_c. A lower coercive means that less energy is required in order to switch states, faster switching speed and lower leakage current, and is thus desired for device implementation [24]. The FE behaviour is characterized by the hysteresis curve of polarization vs external electric field, as exampled in fig. 4(b).

2.3 Deposition processes

TiN was deposited using the sputtering technique. The following description is based on *Sputtering by Particle Bombardment. Experiments and Computer Calculations from Threshold to MeV Energies* [2]. Sputtering takes place in a vacuum chamber to avoid interference from air molecules. The material that is to be deposited, the target, is placed facing the substrate at which the target atoms are to be deposited. An inert gas, most commonly argon, is then introduced to the vacuum chamber. In order to bombard the target with positively charged ions, a strong electrical field is applied to the chamber. This creates a plasma, where an electron separates from the inert gas atom such that a positively charged ion is created. The ions are accelerated by the electric field, bombarding the target such that target atoms are ejected in the direction of the substrate through the transfer of kinetic energy. The sputtered target atoms then reach the substrate, losing their kinetic energy and depositing on the substrate surface. Through controlling the sputtering power, the distance between the substrate and target, and the sputtering time, the thickness of the deposited film can be controlled. The preferential lattice plane orientation (texturing) of the deposited material can also be controlled by alternating the pressure of the inert gas, as done by Athle et al. [4] for controlling lattice plane orientation of TiN. While all lattice planes exist in the sputtered material, the texturing is expressed with regards to the surface normal.

Atomic layer deposition was utilized for deposition of HZO. The following description is based on Khalid [21]. Atomic layer deposition (ALD) is a technique that allows for very precise layer by layer deposition of atoms. The typical ALD cycle consists of first exposing the substrate to chemicals, typically referred to as "precursors" [21]. These react with the substrate, leaving the desired atoms. The byproducts are removed from the chamber in the "purging step". The next precursor is then introduced and the byproducts are purged. This is repeated, introducing the desired precursors and repeating until the wanted film thickness is reached. If the desired end product is an oxide, oxygen can be provided in the form of e.g water during the deposition process.

2.4 Annealing

The following description is based on Humphreys and Hatherly [16]. Annealing is a heat treatment process used to improve the properties of a material. It involves heating up the sample to a certain temperature and then cooling it down under controlled conditions. During deposition processes such as sputtering and ALD, impurities like dislocations, vacancies and grain boundaries tend to form. Through annealing, such defects can be diminished, giving a more uniform crystal structure. The deposited material may also be amorphous, meaning it has no long range order, after the deposition process. The annealing then helps to crystallize the material into a particular crystal structure. There may also be internal stress in the film due to the different thermal expansion between the film and the substrate, and the annealing can prevent eventual damage to the film by relieving that stress. While a high temperature speeds up the crystallisation and grain growth of the film, it is not always appropriate due to implementation purposes. The substrate might be of a material that cannot withstand the high temperature annealing without getting damaged.

Rapid thermal processing (RTP) is an annealing technique that rapidly heats up and cools down the sample on a timescale of seconds to minutes and allows for uniform temperature change across the whole sample. The process also limits the time for phase changes such that the sample is able to crystallize in metastable phases.

2.5   Top electrode deposition

For top electrode deposition, optical lithography was utilized. The following description is based on Lin [25]. Optical lithography is a technique that uses light to define patterns on a desired substrate. First, a mask with the desired electrode pattern is created, such that when light is shone through it the desired pattern is produced. The substrate is then coated with a light sensitive material, a photoresist. Through aligning the sample with the mask and then shining a light through the mask, the electrode pattern is transferred to the substrate. By then using a special solution, either the unexposed or exposed region is removed from the substrate. After the pattern is defined, the electrodes are then deposited. During thermal evaporation the sample which is to be deposited is heated up in vacuum until it vaporizes and is deposited on the substrate. The regions where the photoresist remains are shielded from the deposition, creating the desired electrode pattern.

2.6   HZO compound fraction and annealing

FE behavior has been reported for thin films of several other compounds consisting of HfO_2 with e.g. Si, Y, Al, Gd, Sr instead of Zr [24]. Zr has however proven to have an advantage during the atomic layer deposition (ALD) process. While other compounds allow for only $< 20\%$ compound fraction, Zr has very similar properties to that of Hf which makes a $\sim 50\%$ compound fraction possible [28]. This allows for ALD with alternating precursors Hf and Zr. The 1:1 ratio is much easier to produce homogeneously than the $< 20\%$ doping level of other dopants [28]. Different fractions of Zr has also shown that at a fraction of $\sim 50\%$, ferroelectricity is maximized [30] .

RTP, where the sample is heated up to temperatures of $400 - 1000^{\circ}$ C, has typically been used to achieve the o-phase [29, 30]. Though faster than furnace annealing, this process is still on the timescale of tens of seconds to minutes and thus risks damaging the interface between III-IV semiconductors which would hinder the integration of HZO on such semiconductors [5]. There has thus been investigations into alternative methods to anneal HZO, that would allow for integration in devices reliant on the III-IV semiconductors. One of these has been to lower the annealing temperature to 300-400°C, which has been shown to also crystallize the o-phase [31]. The sample reported in this paper used a 370°C thermal budget [32].

2.7   Stress effects from electrode

As the sandwiched HZO thin film crystallizes, mechanical stress from the top and bottom electrodes may be induced in the HZO. This mechanical stress has through experimental results been shown to be important for the crystallization of the o-phase. Different top and bottom electrodes have been tested, including TiN, RuO_2, Pt, and W. A comparison between the different experimental results of combinations of top and bottom electrodes can be found in Kim et al. [24]. From this data it appears that a TiN top and TiN bottom electrode seems to best crystallize the o-phase.

As mentioned before, the influence of the texturing of TiN has also been studied by Athle

et al. [4]. Through changing the deposition pressure during TiN sputtering, they were able to control the preferential grain orientation between (111) and (002). By then measuring the remanent polarization it was shown that it was much larger for the the (111) orientation.

2.8 Interface effects between film and electrodes

Cycling is the application of consecutive positive and negative electric fields to the device, and is thus inherent to any device. First, a wake-up cycle is always performed in order to initialize the FE behaviour through alignment of the dipoles. It has been shown that wake-up cycling produces oxygen vacancies and crystallite defects at the interface between HZO and TiN [26]. In a device, there would be continued cycling during the lifetime, increasing the number of oxygen vacancies and defects. This would lead to eventual failure [3]. Experimental results however show that the strengthened ferroelectricity from the electrodes is not purely due to stress, but also due to the oxygen vacancies directly contributing to the transition into the o-phase [26]. A compromise between the promotion of the o-phase and the failure resistance thus need to be made. For this purpose, a modified TiN electrode with limited oxygen scavenging behaviour would be ideal [3].

2.9 Film thickness effect

The ferroelectricity of the thin films has been shown to be vastly diminished as the film thickness exceeds 20 nm [22]. This is since the m-phase, which is non-FE, is formed as the film thickness increases. Using a stack of $HZO/Al_2O_3/HZO$, this effect has been diminished and a film of thickness 40 nm can be reached before the film degrades[22]. Riedel et al. [34] have even showed that FE properties could be maintained up to a thickness of 50 nm when the HZO was laminated with Al2O$_3$. Still, the largest reported remanent polarization has been for films of thickness $\sim$ 12 nm [24]. Films of such thickness do not experience tunneling, show high remanent polarization, and is thinner than $Pb(Zr,Ti)O_3$ which is currently in use. While in some cases a thicker film is needed, like in piezoelectric harvester applications, a thin film has both the advantage of having a higher remanent polarization and allowing for down-scaling [24]. Ultrathin ($<$ 3 nm) films are thin enough to be tunneled through, and could be utilized in FE tunneling junctions [24].

3 Method

3.1 X-ray diffraction

The elastic scattering of photons allows for the treatment of the lattice planes as specular reflecting, with the same incoming and outgoing angle [13]. As the sample is exposed to X-rays, they are diffracted off different lattice planes, interfering as their relative phase changes depending on the distance travelled. As evident from fig. 5, the difference in travelled distance is always $2d\sin\theta$, where d is the interplanar distance between the reflecting planes and θ the angle of the beam with regards to the reflecting plane. Constructive interference occurs when the X-ray that has travelled the longer distance is in phase after reflection, meaning the Bragg condition

$$n\lambda = 2d\sin\theta \tag{3}$$

is fulfilled. Here, n is the order of the diffraction and λ the wavelength. As n is just the number of lattice planes the beam has passed through before reflecting, and d is the distance between the uppermost plane and the reflection plane, all orders of diffraction result in the
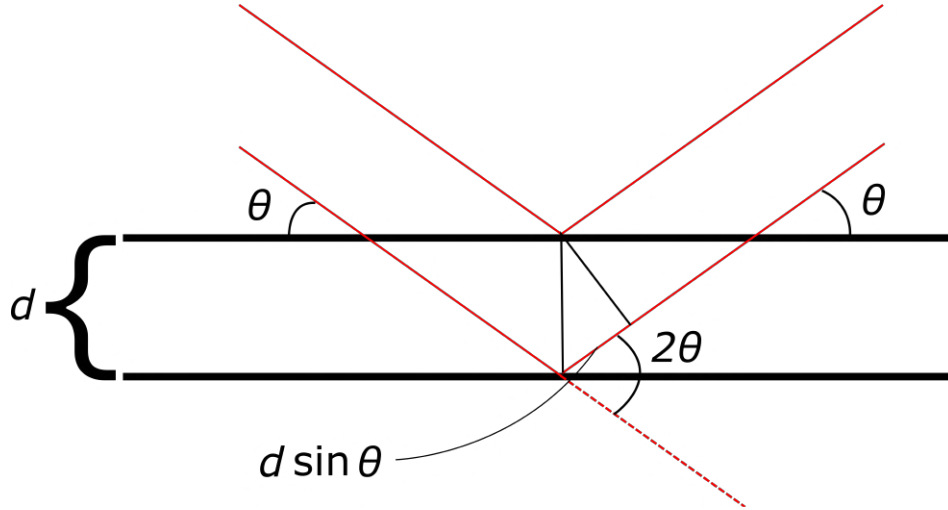
Figure 5: The Bragg reflection geometry. The difference in the travelled distance between the two reflected rays is $2d\sin\theta$. For constructive interference the difference in the travelled distance needs to be an integer multiple of the wavelength.

same θ angle assuming the sample to be a perfect crystal. In order for this to hold, the wavelength needs to be of the same order of magnitude as the interplanar distance as $\sin\theta \leq 1$. As the beam diffracts upon planes with different Miller indices and thus different d, the angle of reflection will be different. Different peaks in the diffraction spectrum can hence be attributed to diffraction off different materials prevalent in the sample, as well as different lattice plane reflections in the same material.

The lattice plane spacing is directly related to the lattice constants through the equation

$$d_o = \frac{1}{\sqrt{\frac{h^2}{|\vec{a}_1|^2} + \frac{k^2}{|\vec{a}_2|^2} + \frac{l^2}{|\vec{a}_3|^2}}} \tag{4}$$

for orthorhombic crystal structure. Note that tetragonal structure is a special case of orthorhombic structure with two lattice constants equal, and similar for cubic with all the lattice constants equal. Since the lattice constant for the cubic Au is slightly smaller than for TiN, we expect the TiN peaks to be slightly to the left of the Au peaks in the 2θ spectrum according to (4) and Bragg's law (3). The monoclinic case is more complicated since not all lattice vectors are orthogonal and as such the interplanar spacing is

$$d_m = \frac{1}{\sqrt{\frac{\left(\frac{h^2}{|\vec{a}_1|^2} + \frac{l^2}{|\vec{a}_3|^2}\right) - 2\frac{hl}{|\vec{a}_1|^2|\vec{a}_3|^2}\cos\beta}{\sin^2\beta} + \frac{k^2}{|\vec{a}_2|^2}}} \tag{5}$$

where β is the angle between $\vec{a}_1$ and $\vec{a}_3$. Through analyzing the diffraction pattern, the crystal structure can thus be reconstructed by matching the pattern with values for the lattice constants and Miller indices that reproduces the correct peak positions. Depending on the crystallite phase, the peak positions in the spectrum will thus differ, giving the ability to analyze the different phases present in the sample through XRD. The crystal also determines the intensity of certain peaks, mathematically described by the structure factor. All ions in the lattice have an ability to scatter X-rays, which diminishes the amplitude of certain reflections due to geometry. Some reflections might even be completely suppressed by ions in the lattice such that peaks can not be found corresponding to that lattice plane. The peaks in this thesis
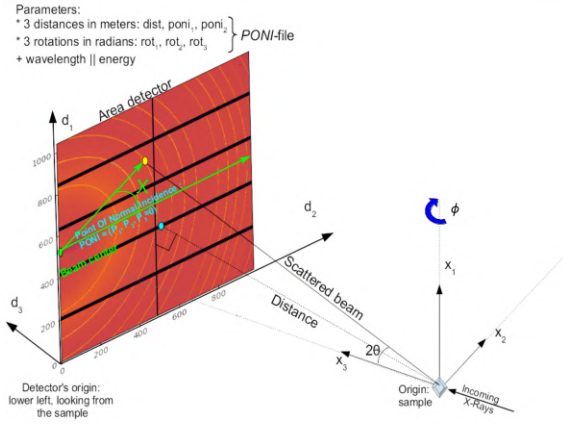
Figure 6: The geometry of the setup, given to the azimuthal integration function in the PONI-file. NanoMAX is able to rotate the sample, the ϕ is the same ϕ as in fig. 1. Both the azimuthal angle χ and the diffraction angle 2θ are shown. Image taken from PyFAI and modified [1].

were identified using Persson et al. [32] as a reference.

If the sample consists of random orientations of lattice planes, the X-rays will reflect in a cone shape, resulting in a diffraction ring pattern when reaching the plane detector. This is the case for powder XRD, where the random orientations of the different powder grains results in reflections in all azimuthal angles. If the sample instead consists of crystallites with an ordered orientation, as is common for thin films, one would expect distinct intensity peaks at certain azimuthal angles. As the angle between the incoming beam and the reflected beam is 2θ (fig. 5), XRD-data is represented with respect to 2θ rather than θ. Through azimuthal integration the diffraction data, which is given as number of counts per pixel position, can be translated to data of the diffraction angle 2θ, and the azimuthal angle χ.

3.2 Azimuthal integration

The azimuthal integration method used here is fully explained in Jensen et al. [19]. The points in the diffraction ring pattern can be represented through polar coordinates, with the azimuthal angle χ being the angle between a reference (horizontal) axis and the line connecting to the data point, and r being the distance to that data point (see fig. 6). This r in real space is proportional to the the 2θ diffraction angle and this distance is as such a measurement of 2θ. Through a so-called PONI (point of normal incidence)-file, the orientation of the experimental setup at the beamline is provided, see fig. 6. Depending on the given PONI-file, the data is assigned to a specific azimuthal angle and radial distance to the beam center. This converts the raw data in fig. 7(a), where the axes are the pixel resolution of the detector, into intensity dependent on χ and the diffraction angle 2θ as seen in fig. 7(b). The intensity dependence on both the scattering and azimuthal angle can then be studied through summing the intensity either along the diffraction or azimuthal angle axis, which is what has been done in fig. 7(c) and (d) respectively.
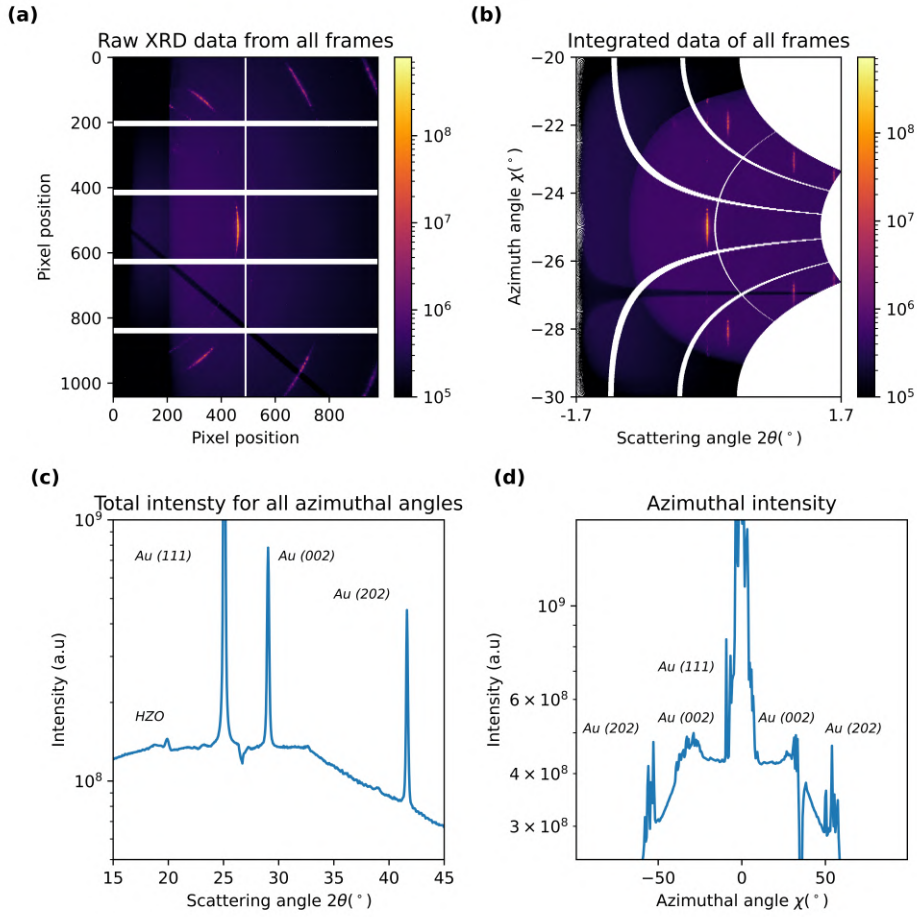
Figure 7: **(a)** Raw XRD data from a fine scan with $\phi = 10^{\circ}$ for all frames. **(b)** Azimuthally integrated raw data. **(c)** The azimuthally integrated data summed over all azimuthal angles. **(d)** The azimuthally integrated data summed over all diffraction angles.

3.3 Grain size

The peaks in a 2θ scan exhibit a Gaussian profile, from which a fit can extract the full width at half maximum (FWHM). One major source of peak broadening is the crystal domain/grain size. A sample consists of several crystalline domains that are all aligned slightly differently to the incoming beam such that the θ angle is slightly different for diffraction of the same lattice plane in different domains. A larger number of small domains leads to a wider spread of diffraction angles which contributes to the width of the peak. The grain size is as such inversely proportional to the FWHM. The relation is fully described by the Scherrer equation:

$$\tau = \frac{K\lambda}{\beta \cos \theta},\tag{6}$$

where τ is the grain size, $K \approx 0.9$ a geometrical constant, β the FWHM purely due to grain size, and λ and θ the wavelength and angle from eq. (3) [14]. This equation provides a lower bound for the grain size as it takes only the broadening from the crystal structure, and not other factors, into account. Eventual microstrain, which thin films often retain, can impact the FWHM, as could instrumental broadening [13]. Still, while not an exact measurement, the Scherrer equation still provides useful information directly from doing a Gaussian fit on the background-subtracted data. In the derivation of the Scherrer equation the grain size is
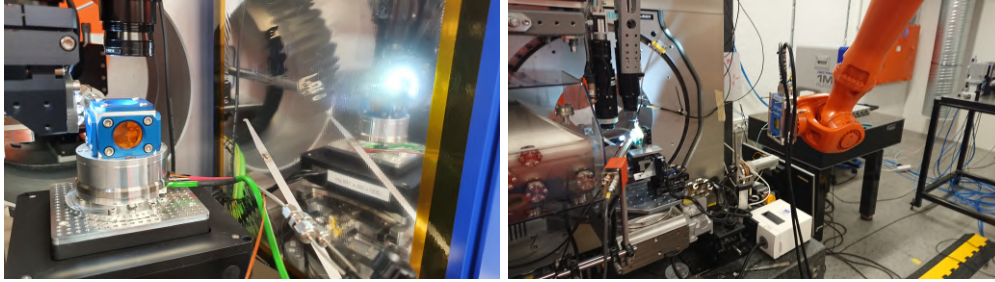
Figure 8: Left: The PILATUS detector with the beamstop at the beam center. Right: Overview of the setup with the incoming beam from the left. Note that the PILATUS detector is not set up in this image.

taken to be $\tau = Nd$ where N is the number of planes and d the interplanar spacing. The name grain size can thus be misleading since what is actually measured is the grain height perpendicular to the surface plane [14].

3.4   NanoMAX beamline and detector

NanoMAX is a beamline at the MAX IV synchrotron facility in Lund, Sweden that allows for a photon energy of $5 - 28$ keV [20]. NanoMAX also has a beam focus of 60 nm-100 nm, allowing for nano-scale study of the sample. Full details of the beamline can be seen in Johansson et al. [20]. Hard X-rays penetrate the sample deeper than soft X-rays, so for the study of thin films the photon energy has to be limited in order to not penetrate the sample without diffracting. High energy (short wavelength) X-rays are however necessary for the study of materials with short interplanar spacing d. This is apparent from Bragg's law (3) since $\sin\theta \leq 1$ implies $n\lambda \leq 2d$. The beamline allows for orientations of the sample through the use of a goniometer, varying the angle between the source, sample surface, and detector [13]. The ϕ-angle rotation is visualized in the illustration in fig. 6. Through the use of a pizeo scanner, the sample can also be moved along the axes.

A PILATUS2 detector, described in Broennimann et al. [6] was utilized. It can be seen in fig. 8. This detector has a 172 μm pixel resolution and 981×1043 detector shape. The detector uses the photoelectric effect for photon counting with each pixel being a detector itself. It consists of a tiled array of sensor modules with gaps between them, as seen in fig. 7(a). These blind spots of the detector are taken into account when performing the azimuthal integration by giving the azimuthal integration a mask which has the shape of the detector blind spots.

3.5   Sample preparation

The sample was prepared according to the process in Persson et al. [32], with some changes. The sample can be seen in fig. 1, and it is also described in tab. 1. The substrate consisted of a 285 μm Si wafer, with an oxidized layer of 2 nm SiO_2. The TiN 10 nm bottom electrode was prepared using sputtering at an argon pressure of 2.7 mTorr. The 12 nm HZO thin film was deposited by utilizing ALD at $200°C$. The utilized precursors were Tetrakis(dimethylamido)hafnium (TDMAHf) and Tetrakis(ethylmethylamido)zirconium (TEMAZr). As the Hf and Zr create a bond with the surface the TDMA and TEMA are removed in the purging step. Water was used as an oxidant during the process. This procedure was exercised until the desired thickness of 12 nm for the HZO was reached. TiN was then sputtered in the same way as the bottom electrode. Annealing was then performed at

Table 1: The prepared sample.

Sample preparation	
Properties	Sample
Annealing process	370°C thermal anneal
Substrate	Si
Bottom electrode	TiN (10 nm)
HZO thickness	HZO (12 nm)
Top electrode	TiN (10 nm)/Au (200 nm)

a temperature of 370°C, calibrated relative to the Au-Si eutectic point $363 \pm 3^{\circ}$C. Thermal evaporation was used to deposit a 200 nm Au layer and excess Au and TiN was removed. The TiN between the Au electrodes was removed using wet etching, a technique in which a liquid chemical solution removes a certain material from the substrate surface. Lastly, the sample was exposed to a square wave with amplitude 3.5 V and a repetition of 1000 times as the wake-up cycle. The samples were also confirmed to display ferroelectricity.

3.6 Data gathering

A 12 keV ($\sim$1 Å) hard X-ray beam was used, which provides good sensitivity to crystal phase and strain. For the calibration of the detector positions, LaB6 powder was used as its diffraction pattern is well known with precise peak positions. Several scans varying in position and ϕ-angles were performed on the HZO. After inspection the fine scan with the angle $\phi = 10^{\circ}$ with respect to the surface was deemed to display the strongest HZO diffraction and is thus further studied in this paper. This scan was from x-position -1.7 μm to 1.7μm with 81 steps, and from y-position -30 μm to -20 μm with 41 steps. The x-resolution is thus higher than the y-resolution. Since the sample is at an angle with respect to the incoming beam, the position in x does not describe the positing in the sample which is retrieved by multiplying x by a factor $\frac{1}{\sin(10^{\circ})}$.

4 Results

4.1 Scan maps

In a scan the piezo-scanner is used such that the sample position changes some distance during some time and the beam diffracts upon different regions of the sample, and diffraction data is registered for every such point. If one parameter is chosen to represent one frame (this could for instance be the intensity of the frame or the FWHM of a certain peak), one can represent the data through a scan image. This allows for different regions of the sample to be categorized, as visible in figure 9. In this image the total intensity of the scan is chosen as a parameter and it indicates that there is more diffraction in certain regions than others. If there is diffraction on the contact (top electrode), several high intensity Au peaks and more background will appear in the data, which will increase the total intensity of the frame. This effectively creates a real space image of the sample, where the high intensity regions indicate where the Au electrode is located. This can then be utilized to study the highly diffracting (on-contact) regions separately, as well as observing previously very weak peaks in the lower intensity (off-contact) regions. The separation of the on-contact and off-contact scans has been made in fig. 9(b), where thresholds for what is deemed off- and on-contact have been set. The white region contains intensity frames higher than 55% of the highest intensity frame and is deemed to be on-contact, while the black region contains frames with lower than 25% of
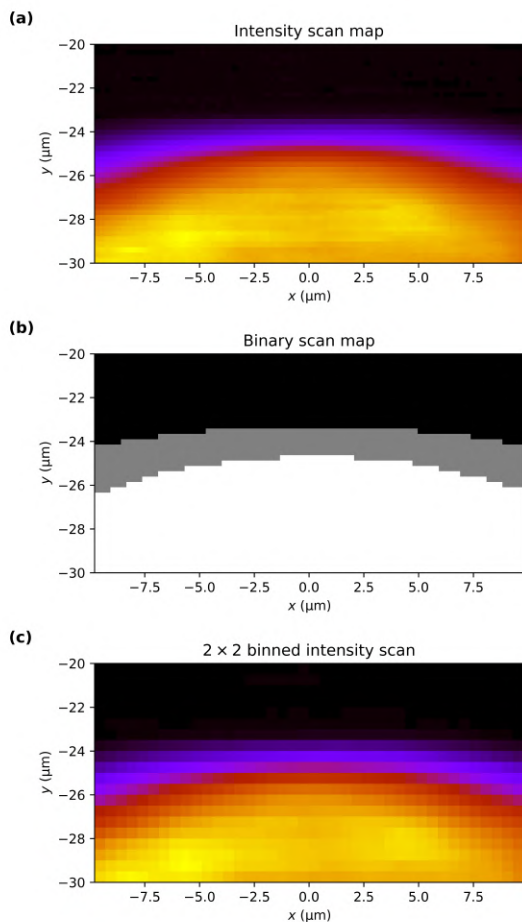
Figure 9: **(a)** Scan map of the intensity for all frames. **(b)** Binary scan map used to determine what is on-contact and off-contact. The white is on-contact, the grey is the edge-region, and the black is off-contact. The threshold for off contact was set to be 25% of the intensity of the highest total intensity frame, while the threshold for on-contact was set to 55% of the intensity of the highest total intensity frame. **(c)** A 2×2 binned scan map of (a).

the highest intensity frame and is deemed to be off-contact. The gray region is for intensities between 25% and 55% and is set as neither on- nor off-contact. The diffraction intensities from all off-contact frames are summed and the same is done for the on-contact frames. Summing up these intensities along the azimuthal angle results in the the two intensities in fig. 10, where the off-contact intensity has been scaled to the same intensity as the on-contact intensity.

The individual frames might however have too low signal to noise ratio do any meaningful data analysis on. Through binning the close-lying scan frames are combined into one bin that then has a lower signal to noise ratio. This was utilized to create (2×2) binning of the frames, as seen in fig. 9(c).

4.2 Background removal

For further analysis, the binned frames were used since the data has been averaged over four frames and is thus easier to work with, while still being able to distinguish between the regions. After binning, additional background subtraction is required to analyze the
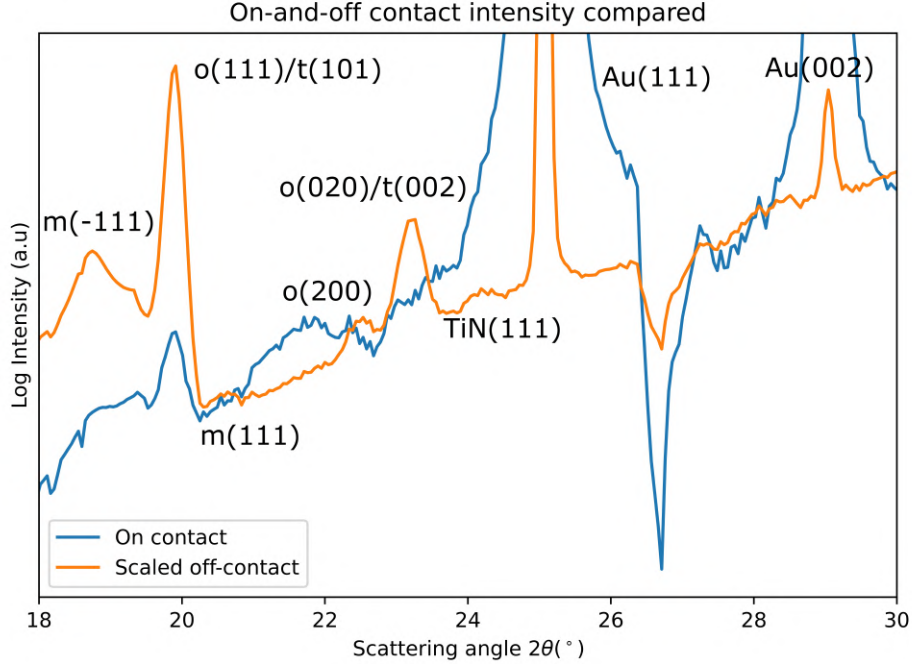
Figure 10: On-contact compared with off-contact intensity. The off-contact intensity is scaled by a factor $1.7 \cdot I + 2\theta \cdot 1.5 \times 10^3$ where I is the real intensity.

spectra, and traditional polynomial background subtraction is not suitable. For this purpose pybaselines [11], which is a python library that provides several different types of baseline correction algorithms, was used. After extensive testing of the different methods provided by pybaselines, the morphological ones were deemed to be the most satisfactory. According to pybaselines, these use moving windows in which the maximum and minimum are computed, as well as a combination of the two [11]. Four examples of background removal can be seen in figs. 11(a) and (c) for an off-contact and on-contact bin respectively. Of these, the rolling ball background removal was deemed to be the most consistent when used for all bins and was therefore used for all succeeding background removal. It was found that limiting the 2θ region for which the background was fitted also helped to make the fit more consistent.

4.3   Gaussian fitting in the 2θ spectrum

The background removal allowed for Gaussian fitting to be performed on the o(111)/t(101) HZO peak. This was done using a Gaussian fitting function based on curve fit from SciPy [37]. The orthorhombic peak aligns with the t(101) peak and they can thus not be distinguished from each other, while the wider m(-111) peak has a slightly smaller diffraction angle. Fitting accurately to the o/t peak with a single Gaussian still proved to be difficult, as the fit was influenced by the m-peak. A double Gaussian fit was thus utilized in order to better extract the peak position and FWHM for the o/t peak. A comparison between the double and single fit for both the on- and off-contact bins can be seen in fig. 12. While the fits for the on-contact bins are identical both in position and FWHM up to the fourth significant figure, the on-contact fits for the single bins is both shifted to the left and has a FWHM that is too large.

This fitting was performed for all bins, in order to create scan maps of the peak position and FWHM. The fitting function requires an initial guess for the position of the peaks as
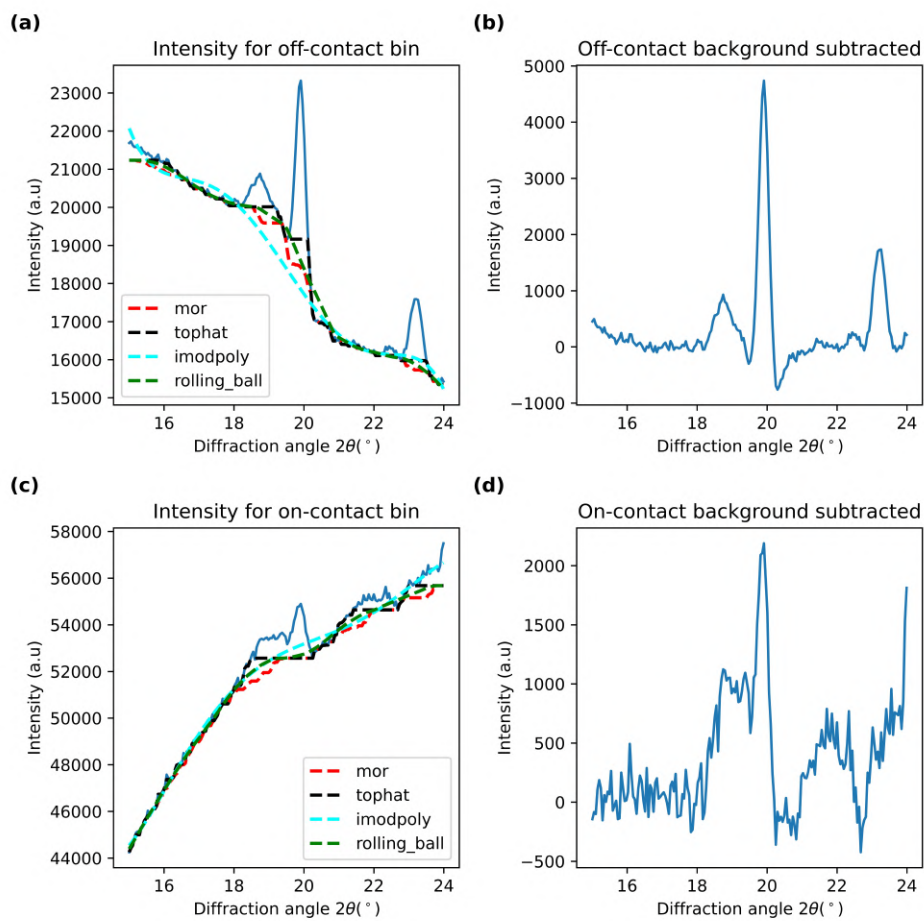
Figure 11: **(a)** Off-contact bin intensity with different baseline removal functions. **(b)** Intensity for the same bin as in (a) with the rolling ball background subtracted. **(c)** On-contact bin intensity with different baseline removal functions. **(d)** Intensity for the same bin as in (c) with the rolling ball background subtracted.
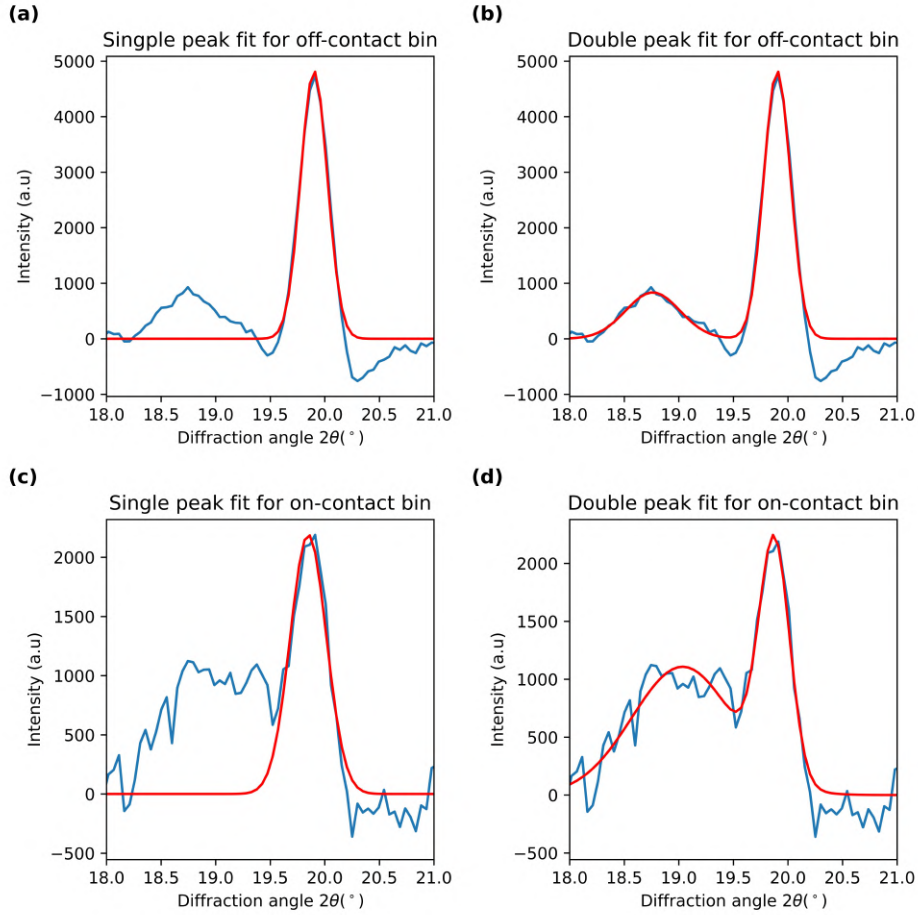
Figure 12: **(a)** Single peak fit for off-contact bin with peak position at $2\theta = 19.90^{\circ}$ and FWHM=0.2880°. **(b)** Double peak fit for off-contact bin with peak position at $2\theta = 19.90^{\circ}$ and FWHM=0.2880°. **(c)** Single peak fit for on-contact bin with peak position at $2\theta = 19.85^{\circ}$ and FWHM=0.3909°. **(d)** Double peak fit for off-contact bin with peak position at $2\theta = 19.88^{\circ}$ and FWHM=0.3292°.
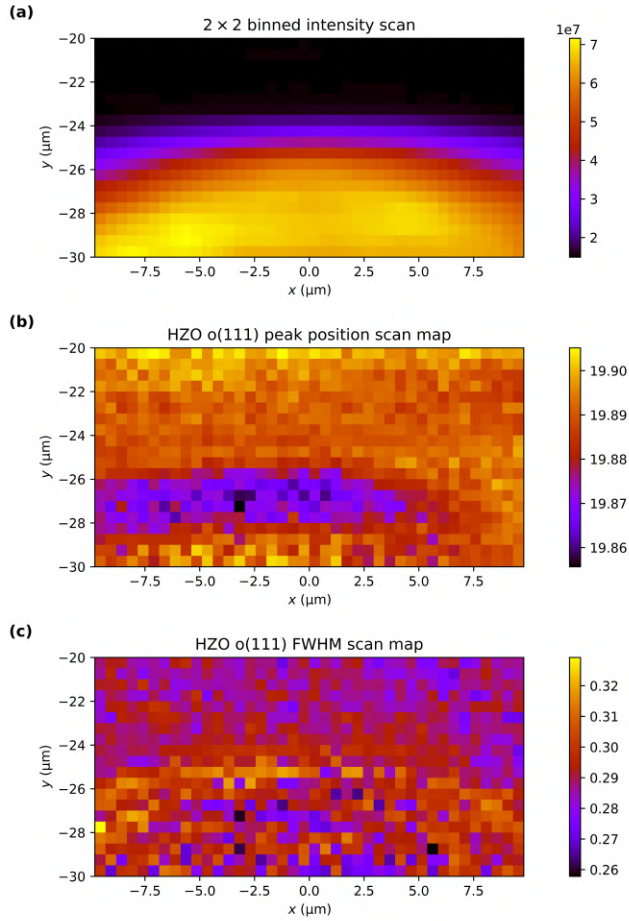
Figure 13: **(a)** Binned intensity scan map used for comparison with the peak position and FWHM scan maps. **(b)** Position scan map of the HZO o/t peak from the double fit. **(c)** FWHM scan of the HZO o/t peak from the double fit.

well as the number of points around that point that the fit will take into consideration. If these given parameters are not enough for the fit to work, the fitting will fail. This proved to be a problem as the double fitting function required different initial guesses and different number of points to be taken into account. In order to obtain a fit for all bins, different initial guesses and number of points taken into consideration were given, until a correct fit could be found. Restrictions on the peak positions were also set in order to not have any fitting to the wrong peak. Scan maps were created both for the FWHM and the peak position using this double fit. While the double fitting improved the results, there is still a region whose peaks are generally shifted to the left. While the background removal process may result in a slightly shifting peak position that may vary for different frames/bins depending on how well the fit works, the resulting scan map can not be fully attributed to that. Investigating the most left-shifted peak position, it can be seen that Gaussian has fitted correctly to the peak.
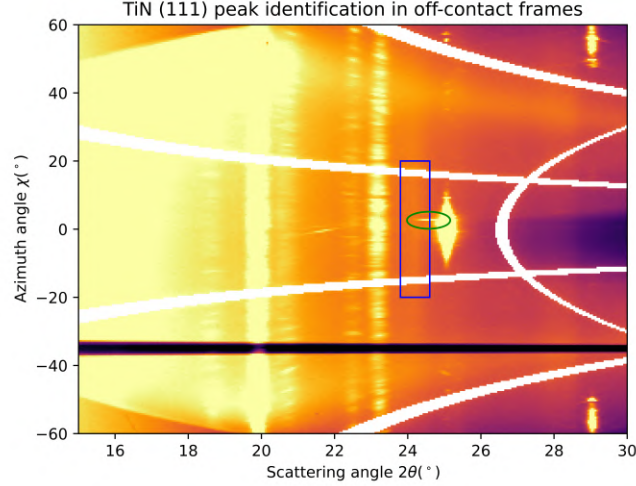
Figure 14: Peak identifying of TiN(111) in the azimuthally integrated data of the off-scan frames. The blue box indicates where the peak is and the green ellipse marks the Au streak.
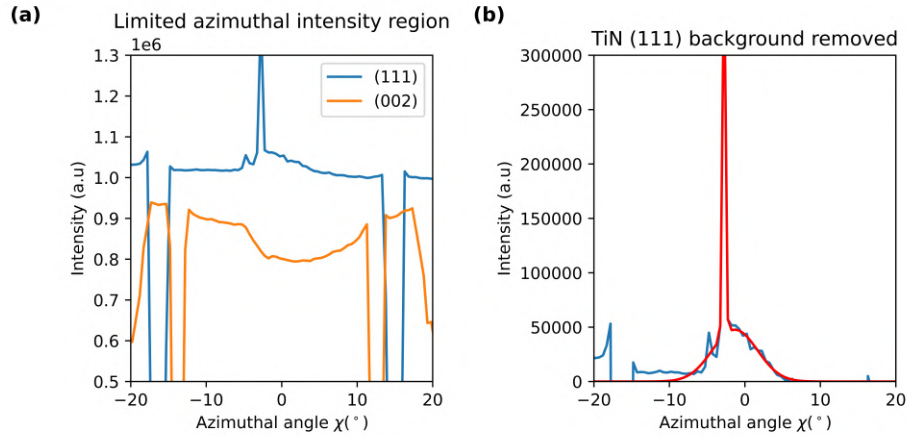

Figure 15: **(a)** Azimuthal angle intensity for the off-contact frames from the around the (111) and (002) expected peak locations. **(b)** Double Gaussian fit in order to quantify spread of azimuthal angles.

4.4 TiN fitting

The azimuthal intensity (fig. 7(d)) was separated into on-contact and off-contact scans using the binary scan map (fig. 9(b).) Since the background and the Au peaks mask the TiN peaks in the on-contact scan, only the off-contact scans were analyzed. The peak positions expected for TiN(111), (002), and (202) were $24.36°$ and $28.20°$ and $40.31°$. As such, the region of these values $(\pm 0.4°)$ were summed up along 2θ such that eventual texturing could be detected. The (111) peak can be observed, although very vaguely, in fig. 14. The azimuthal intensity around the expected 2θ peak positions of the (111) and (002) reflections can be seen fig. 15(a). The TiN(111) peak is here more clearly observed than in fig 14, while no (002) peak could be observed, as was the case for (202). A Gaussian fit was performed on the TiN(111) peak in order to determine the peak position and the FWHM. The narrow peak was deemed to be a diffraction extending from the Au region, as seen in fig. 14, and thus a double Gaussian was

utilized in order to only extract the FWHM from the relevant TiN(111) peaks (fig. 15(b)). The peak position determined from the fit was $\chi = -1.33^{\circ}$ and the FWHM was 7.02°.

5 Discussion

5.1 Regional studying of sample

The peak position scan map (fig. 13(b)) has a region that differentiates itself from the rest of the sample. Comparing it to the intensity scan map (fig. 13(a)), it can be observed that this region is on-contact. Observing the diffraction angle spectrum of these left-shifted peaks, the fits are indeed correct. While some peak-position variation can arise from uneven background removal, the magnitude of the peak shifting, as well as the restricted region can not be explained by this. It is important to also note that the annealing conditions where the same for the whole sample, as the TiN between the top electrodes was wet-etched after annealing was performed. Since the left-shifted region is not distributed over the whole on-contact region, the interaction between the TiN top electrode and the HZO thin film is not uniform over the whole sample. From Bragg's law (3) we have that the peak position $2\theta \propto \sin^{-1}\left(\frac{1}{d}\right)$. Any increase in d would thus lead to a shifting of the peak to a lower 2θ value. If the peak shifting is purely due to strain, a $2\theta \sim 0.03^{\circ}$ shifting from $\sim 19.90^{\circ}$ to $\sim 19.87^{\circ}$, would correspond to a strain of $\varepsilon \sim 0.15\%$ in d. Since this is in the on-contact region, there could be strain from the top electrode.

Another source of peak-shifting is oxygen vacancies which would change the lattice parameters. The sample underwent a wake up sequence 1000 times, during which such oxygen vacancies could have been created. The distribution of such oxygen vacancies is not necessarily uniform over the whole sample and would explain why the shifting is only seen in a certain region.

The fact that the peak arises both from the o- and t-phase might also be a factor. The t-phase peak has a larger peak position value than the o-phase by a factor $\Delta 2\theta \sim 0.25$ [4]. If more of the HZO were to crystallize in the o-phase and less in the t-phase, this would shift the peak to the left. Since the peaks can not be distinguished it is not possible to tell how much of o-phase or t-phase there is in different regions of the sample from this peak. There are also other, less intense reflections from the o-phase, but these either align with t-phase or m-phase peaks and can thus not give any new information [30]. Since the peak shifting can not possibly be larger than the peak separation, the shifting can not be explained fully by a phase transition, but together with the other reasons given above the phenomena can be explained.

The FWHM scan map (fig. 13(c)) displays a generally even spread of values around FWHM$\sim 0.29^{\circ}$. There is however a definite increase in the edge region between the on-contact and off-contact region where the FWHM$\sim 0.31^{\circ}$. What this shows is a wider spread of lattice plane orientations in this region, resulting in a larger spread of diffraction angles. From the Scherrer equation (6), this corresponds to larger grains which could be from some interaction with the top electrode. Microstrain induced in the sample also contributes to the FWHM according to $\beta_{\varepsilon} = 4\varepsilon \cos \theta$, where ε is the microstrain [13]. There could be some induced microstrain in this edge region due to macrostrain between the edge region of the top electrode and the HZO, although no peak-shifting is observed.

5.2   Comparing on- and off-contact scans

The on- and (scaled) off-contact intensities are compared in fig. 10. It is important to note that the prevalence of a peak in this comparison does not imply that the corresponding phase is more prevalent in the off-contact region. The background is simply much higher in the on-contact region, limiting the visibility of smaller peaks.

The m-peak can be distinguished in both the on-contact and off-contact scan. This demonstrates that even though the sample was processed with the intention of maximizing the crystallisation in the o-phase, there is still m-phase present, though enough o-phase coexists for the film to exhibit FE performance. The m-phase is expected to be prevalent due to the temperature during the annealing procedure being on the low end of what is required to produce the o-phase.

The Au peaks are way more intense in the on-contact, which results in buried TiN peaks. The Au peaks are still observed in the off-contact intensity as the thickness of the top electrode makes the tails of the X-rays sensitive to it. In the off-contact scan we see a small peak that can be attributed to a (111) reflection off TiN, which is expected to be around $24.36°$. The (002) and (202) peaks are expected to be around $28.20°$ and $40.31°$ respectively, but both of these are either too weak to be observed or the corresponding texturing is not present in the film. There are two distinct peaks around $2\theta \sim 23°$ in the off-contact intensity, that can not be distinguished in the on-contact intensity. In these regions, we would expect to find several peaks, with the most intense being from diffraction off two other o-phase planes [32]. These peaks are likely buried in the on-contact intensity, as the peaks are less intense than the o/t-peak at $2\theta \sim 19.9$ and closer to the Au peak.

5.3   Grain size analysis

From the Gaussian fits, using the Scherrer equation (6) an approximate grain size of the HZO can be deduced. For the double fitting at the HZO o/t peak, taking the average of the scan map values and using the Scherrer equation results in an average crystallite size of $\tau \sim 19$ nm. As discussed in the theory, the width β in the Scherrer equation is taken to arise purely from the crystallite size. There are however many other factors in the peak broadening. One of these is that the peak is a result of scattering both from the o- and t-phase whose peak positions differ by about $\sim 0.2°$ on the 2θ spectrum.

This does however do the opposite of explaining the fact that the Scherrer equation results in a larger size than the thickness of the film. Observing the peak for both the on-and off-contact intensities in fig. 10, it can be observed that the FWHM$\sim 0.3°$, so the FWHMs in fig. 13 are indeed correct and such a small FWHM results in a minimum crystallite size of ~ 19 nm. While the shape factor K varies depending on the crystallite shape, even taking the minimum reported value for the shape factor, $K = 0.62$ only results in a crystallite domain size of ~ 13 nm [14]. If the grain size is larger than the thickness of the film, the Scherrer equation should just measure the thickness of the film [14]. As such the the equation is not applicable for grain size measurement in the thin HZO film. This still does not explain the fact that the it returns a value that is larger than the film thickness itself. In the derivation of the Scherrer equation it is assumed that $\tau = Nd$ where N is the number of planes and d the interplanar spacing [14]. In an article published in Nature, Cho et al. [9] analyzed an HZO film of thickness 12 nm. Using the Scherrer equation, they found grain sizes exceeding the thickness of the film. This inconsistency was however not noted in the article. This demonstrates that there is some underlying reason that makes the Scherrer equation. not apply in these thin HZO film XRD

measurements. Additionally, the use of a focused X-ray nanoprobe complicated the Scherrer analysis, as most XRD measurements utilize μm or mm sized X-ray spots.

The grain size depends upon a number of factors from the production method, including the annealing temperature, annealing time, film thickness and pressure during the ALD [8][9]. To analyze the grain size of the samples, atomic force microscopy (AFM) could be used. AFM uses a sharp cantilever with a sharp tip at the end. When a laser is reflected on the cantilever and the cantilever moves from interacting with the sample, the reflection angle will change slightly. Letting the reflected beam hit a photodetector, the movements of the reflected beam are registered. As these movements are correlated with the topography of the sample, it can be used to image the grains present [38]. It is important to note that these measurements are of the grain size parallel to the plane and not perpendicular, as in the X-ray diffraction. These grain sizes can as such be larger than the film thickness if the grains are anisotropic. AFM was used by Chen et al. [8] for grain size measurements of several different samples annealed at different temperatures, with different annealing times, and of different film thickness. The grain size was shown to increase for higher annealing temperatures, longer annealing times, and thicker films. The remanent polarization was shown to decrease monotonically from 25.6 $\mu C/cm^2$ to 5.35 $\mu C/cm^{-2}$ with the increase of the average grain size from 20 nm to 45.3 nm. The results agree with the fact that ~ 10 nm films display the highest remanent polarization [24]. Smaller grains contribute to a large surface energy, helping to crystallize in the o-phase.

5.4 Texturing analysis

There was very little observed diffraction off the TiN. From 15(b) we have that $\chi = -1.33^{\circ}$ for the diffraction off the (111) plane. Because the planes are not perfectly aligned, there is diffraction off several lattice planes in different grains and as such several peaks at slightly different azimuthal angles because of the different alignments to the beam. This spread of azimuthal angles result in a FWHM of 7.02°. Since this is the only observed peak around an azimuthal angle of $\chi = 0^{\circ}$, it demonstrates that the TiN bottom electrode is (111) textured. From the Miller indices, the angles between the planes can be calculated. Between the (111) plane and the (002) plane the angle is $\chi_{002} = 54.74^{\circ}$ and between the (111) plane and (202) plane it is $\chi_{202} = 35.26^{\circ}$. The diffraction off the (111) plane is at azimuthal angle $\chi = -1.33^{\circ}$ and the other peak positions would thus be expected to be found at $-1.33^{\circ} \pm 54.74^{\circ}$ and $-1.33^{\circ} \pm 35.26^{\circ}$ respectively. There are however no observed peaks in these regions, indicating that there are no reflections off the (002) or (202) TiN planes, or these reflections are too weak to be observed. The fact that the very weak (111) peak should be the highest intensity peak, since the TiN is (111) textured, agrees with this.

It has been shown that the (111) textured TiN achieves a higher remanent polarization than (002) textured TiN [4]. This could possibly be explained by the different strain they induce on the HZO during the crystallization process. TiN with (111) texturing induces a tensile stress while (002) texturing results in compressive stress [33]. The induced in-plane stress in the HZO would allow for the m-phase to better transform into the o-phase and thus increase the ferroelectric behavior. When depositing TiN through sputtering, the pressure during the process can suppress the (002) texturing. Athle et al. [4] found sputtering at a pressure of 2.6 mTorr reduced the (002) texturing significantly. The electrodes studied here were sputtered at an argon pressure of 2.7 mTorr. The measuring of the preferred (111) orientation thus agrees with what was found by Athle et al. [4]. What is interesting to note is that they also found that if the sputtering pressure was increased further, to 4.0 mTorr, both the (111) and (002) diffraction intensities decreased, indicating overall less crystallinity of the TiN electrode. The

preferred orientation is decided by the low strain energy of the (111) orientation and the low surface energy of the (002) plane [17]. The pressure during the deposition process influences this as (moderately) high pressure makes the strain energy dominate while the surface energy dominates at low pressures [33]. The sputtering process used for the studied thermally annealed sample has thus been shown to result in primarily (111) textured TiN, which is ideal for the creation of the FE o-phase[4].

6   Summary and outlook

In this thesis, the FE o-phase of HZO has been studied using nano-focused hard X-ray diffraction, demonstrating that it is possible to use this technique to study thin HZO films. The regional diffraction spectra made possible by the nanoprobe imaging all display peaks that can be attributed to diffraction off the o-phase, which would explain the ferroelectricity displayed by the sample. Analyzing the peak position of the o(111) peak from this imaging it can be observed that the crystallization of the sample is not uniform, with a larger interplanar spacing d in a region of the sample. This can be attributed to a number of different factors, such as strain, oxygen vacancies, or a larger t-phase fraction in this region. Extracting the FWHM of the same peak, it could be seen that there is a general increase in the edge region of the top electrode. From the Scherrer equation this would mean a smaller orthorhombic grain size. The grain size from the Scherrer equation is however larger than the film thickness itself in all regions of the sample. This is not something that can be explained but has been observed previously [9]. No peaks that can be attributed to TiN can be observed for the on-contact diffraction spectrum, due to the higher intensity Au peaks making possible TiN peaks non-discernible. As such no conclusions about the crystalline structure of the top electrode can be drawn. In the off-contact diffraction spectrum a TiN(111) peak can be observed and since no other peaks that can be attributed to the TiN are discernible, this demonstrates that the TiN bottom electrode seems to be (111) textured. For the sputtering pressure of 2.6 mTorr utilized in this thesis, this is the expected texturing, and it is also ideal for HZO crystallization in the o-phase [4]. The analysis was as such successful in studying the regional phenomena of the HZO, as well as the texturing of the TiN bottom electrode, but the high Au peak intensity made the TiN top texturing impossible to observe.

Due to time limits, analysis was only performed on one scan. Several different scans were carried out during the beamtime, which might reveal other properties of the sample. These include scans on other contacts as well as scans in which the goniometer angle ϕ is varied instead of the position. From these ϕ varying scans, increases and decreases in the TiN peak intensities as ϕ varies could be used to further classify the texturing [13]. Grain size measurements using other, more precise techniques, could also be made. In order to better study films by means of XRD, no Au top electrode should be deposited. In particular, the texturing could be studied properly without any high intensity Au peaks burying other peaks.

During the beamtime, a laser annealed sample with a Si/Tin (10 nm)/HZO (3.5 nm)/W (10 nm) stack from Athle et al. [5] was also analyzed. Due to the thin HZO film the intensity of the the HZO peaks was significantly lowered and as such the analysis proved to be more difficult. Further analysis of this sample could provide insight into an alternative processing condition for HZO, that has a lower thermal budget than thermally annealed samples [5].

7 Acknowledgements

References

[1] Fast azimuthal integration using python. `https://pyfai.readthedocs.io/en/v2023.1/`. Accessed: 2023-12-10.

[2] *Sputtering by Particle Bombardment. Experiments and Computer Calculations from Threshold to MeV Energies.* Topics in Applied Physics: 110. Springer Berlin Heidelberg, 2007. ISBN 9783540445005. URL `https://ludwig.lub.lu.se/login?url=https://search.ebscohost.com/login.aspx?direct=true&AuthType=ip,uid&db=cat02271a&AN=atoz.ebs373424e&site=eds-live&scope=site`.

[3] R. Alcala, M. Materano, P.D. Lomenzo, P. Vishnumurthy, T. Mikolajick, U. Schroeder, W. Hamouda, C. Dubourdieu, N. Barrett, and A. Kersch. The electrode-ferroelectric interface as the primary constraint on endurance and retention in hzo-based ferroelectric capacitors. *Advanced Functional Materials*, 33 (43), 2023. ISSN 16163028. URL `https://ludwig.lub.lu.se/login?url=https://search.ebscohost.com/login.aspx?direct=true&AuthType=ip,uid&db=edselc&AN=edselc.2-52.0-85163209465&site=eds-live&scope=site`.

[4] R. Athle, A.E.O. Persson, H. Menon, M. Borg, A. Irish, and R. Timm. Effects of tin top electrode texturing on ferroelectricity in hf1- xzrxo2. *ACS Applied Materials and Interfaces*, 13(9):11089–11095 – 11095, 2021. ISSN 19448252. URL `https://ludwig.lub.lu.se/login?url=https://search.ebscohost.com/login.aspx?direct=true&AuthType=ip,uid&db=edselc&AN=edselc.2-52.0-85102965332&site=eds-live&scope=site`.

[5] Robin Athle, Theodor Blom, Austin Irish, Anton E.O. Persson, Lars Erik Wernersson, Rainer Timm, and Mattias Borg. Improved endurance of ferroelectric hfxzr1–xo2 integrated on inas using millisecond annealing. *Advanced Materials Interfaces NanoLund: Center for Nanoscience*, 9(27), 2022. ISSN 2196-7350. URL `https://ludwig.lub.lu.se/login?url=https://search.ebscohost.com/login.aspx?direct=true&AuthType=ip,uid&db=edsswe&AN=edsswe.oai.lup.lub.lu.se.c75088eb.ec5a.4a1f.97e8.1f493d1e16c1&site=eds-live&scope=site`.

[6] Ch. Broennimann, E. F. Eikenberry, B. Henrich, R. Horisberger, G. Huelsen, E. Pohl, B. Schmitt, C. Schulze-Briese, M. Suzuki, T. Tomizaki, H. Toyokawa, and A. Wagner. The pilatus 1m detector. *Journal of Synchrotron Radiation*, 13(2):120 – 130, 2006. ISSN 09090495. URL `https://ludwig.lub.lu.se/login?url=https://search.ebscohost.com/login.aspx?direct=true&AuthType=ip,uid&db=edb&AN=20331326&site=eds-live&scope=site`.

[7] T. S. Böscke, J. üller, D. Bräuhaus, U. Schröder, and U. Böttger. Ferroelectricity in hafnium oxide thin films. *Applied Physics Letters*, 99(10), 2011. URL `https://ludwig.lub.lu.se/login?url=https://search.ebscohost.com/login.aspx?direct=true&AuthType=ip,uid&db=inh&AN=12380735&site=eds-live&scope=site`.

[8] Haiyan Chen, Hang Luo, Xi Yuan, and Dou Zhang. Constructing a correlation between ferroelectricity and grain sizes in hf0.5zr0.5o2 ferroelectric thin films. *CrystEngComm*, 24:1731–1737, 2022. doi: 10.1039/D1CE01626A. URL `http://dx.doi.org/10.1039/D1CE01626A`.

[9] H.W. Cho, P. Pujar, S. Hong, J. Park, S. Baek, S. Kim, M. Choi, J. Lee, S. Kang, and Y. Kim. Direct growth of orthorhombic hf0.5zr0.5o2 thin films for hysteresis-free mos2 negative capacitance field-effect transistors. *npj 2D Materials and Applications*, 5(1), 2021. ISSN 23977132. URL `https://ludwig.lub.lu.se/login?url=https://search.ebscohost.com/login.aspx?direct=true&AuthType=ip,uid&db=edselc&AN=edselc.2-52.0-85104690576&site=eds-live&scope=site`.

[10] Ronald E. Cohen. Origin of ferroelectricity in perovskite oxides. *Nature (London)*, 358 (6382):136 – 138, 1992. ISSN 00280836. URL `https://ludwig.lub.lu.se/login?url=https://search.ebscohost.com/login.aspx?direct=true&AuthType=ip,uid&db=geh&AN=1992-031720&site=eds-live&scope=site`.

[11] Donald Erb. pybaselines: A Python library of algorithms for the baseline correction of experimental data. URL `https://github.com/derb12/pybaselines`.

[12] Dominik Fischer and Alfred Kersch. The effect of dopants on the dielectric constant of hfo2 and zro2from first principles. *Applied Physics Letters*, 92:012908–012908, 01 2008. doi: 10.1063/1.2828696.

[13] George F. Harrington and José Santiso. Back-to-basics tutorial: X-ray diffraction of thin films. *Journal of Electroceramics*, 47(4):141 – 163, 2021. ISSN 1385-3449. URL `https://ludwig.lub.lu.se/login?url=https://search.ebscohost.com/login.aspx?direct=true&AuthType=ip,uid&db=edssjs&AN=edssjs.2FBC1A09&site=eds-live&scope=site`.

[14] K. He, N. Chen, C. Wang, L. Wei, and J. Chen. Method for determining crystal grain size by x-ray diffraction. *Crystal Research and Technology*, 53(2), 2018. ISSN 15214079. URL `https://ludwig.lub.lu.se/login?url=https://search.ebscohost.com/login.aspx?direct=true&AuthType=ip,uid&db=edselc&AN=edselc.2-52.0-85040641583&site=eds-live&scope=site`.

[15] Philip Hofmann. *Solid state physics —an introduction—2nd ed (Physics textbook)*. Wiley-VCH Verlag GmBH, n.d. ISBN 9783527412822. URL `https://ludwig.lub.lu.se/login?url=https://search.ebscohost.com/login.aspx?direct=true&AuthType=ip,uid&db=cat02271a&AN=atoz.ebs4195707e&site=eds-live&scope=site`.

[16] F. J. Humphreys and M. Hatherly. *Recrystallization and related annealing phenomena.* Elsevier, 2004. ISBN 9780080441641. URL `https://ludwig.lub.lu.se/login?url=https://search.ebscohost.com/login.aspx?direct=true&AuthType=ip,uid&db=cat02271a&AN=atoz.ebs353606e&site=eds-live&scope=site`.

[17] Morteza Jafarzadeh, Kaykhosrow Khojier, and Hadi Savaloni. Influence of nitrogen gas flow on mechanical and tribological properties of sputtered chromium nitride thin films. In *Ultrafine Grained and Nano-Structured Materials IV*, volume 829 of *Advanced Materials Research*, pages 497–501. Trans Tech Publications Ltd, 1 2014. doi: 10.4028/www.scientific.net/AMR.829.497.

[18] Anubhav Jain, Shyue Ping Ong, Geoffroy Hautier, Wei Chen, William Davidson Richards, Stephen Dacek, Shreyas Cholia, Dan Gunter, David Skinner, Gerbrand Ceder, and Kristin A Persson. Commentary: The materials project: A materials genome approach to accelerating materials innovation. *APL Materials*, (1), 2013. URL `https://ludwig.lub.lu.se/login?url=https:`

//search.ebscohost.com/login.aspx?direct=true&AuthType=ip,uid&
amp;db=edssch&AN=edssch.oai%3aescholarship.org%3aark%3a%2f13030%
2fqt3h26p692&site=eds-live&scope=site.

[19] Alexander Bernthz Jensen, Thorbjørn Erik Køppen Christensen, Clemens Weninger, and Henrik Birkedal. Very large-scale diffraction investigations enabled by a matrix-multiplication facilitated radial and azimuthal integration algorithm : Matfraia. *Journal of Synchrotron Radiation eSSENCE: The e-Science Collaboration*, 29:1420 – 1428, 2022. ISSN 1600-5775. URL https://ludwig.lub.lu.se/login?url=https://search.ebscohost.com/login.aspx?direct=true&AuthType=ip,uid&db=edsswe&AN=edsswe.oai.lup.lub.lu.se.96a48763.af4e.4e11.b3ab.5f8c33632ebd&site=eds-live&scope=site.

[20] Ulf Johansson, Dina Carbone, Sebastian Kalbfleisch, Alexander Björling, Maik Kahnt, Simone Sala, Tomas Stankevic, Marianne Liebi, Angel Rodriguez Fernandez, Björn Bring, David Paterson, Karina Thanell, Paul Bell, David Erb, Clemens Weninger, Zdenek Matej, Linus Roslund, Karl Ahnberg, Brian Norsk Jensen, Hamed Tarawneh, Anders Mikkelsen, and Ulrich Vogt. Nanomax : The hard x-ray nanoprobe beamline at the max iv laboratory. *Journal of Synchrotron Radiation NanoLund: Centre for Nanoscience*, 28:1935 – 1947, 2021. ISSN 0909-0495. URL https://ludwig.lub.lu.se/login?url=https://search.ebscohost.com/login.aspx?direct=true&AuthType=ip,uid&db=edsswe&AN=edsswe.oai.lup.lub.lu.se.f974f8cb.f15e.49ef.8802.311b3a21c77f&site=eds-live&scope=site.

[21] Hattar Khalid. *Atomic Layer Deposition. [Elektronisk resurs].* MDPI AG, 2020. ISBN 9783039366521. URL https://ludwig.lub.lu.se/login?url=https://search.ebscohost.com/login.aspx?direct=true&AuthType=ip,uid&db=cat07147a&AN=lub.6865813&site=eds-live&scope=site.

[22] H.J. Kim, M.H. Park, Y.J. Kim, Y.H. Lee, W. Jeon, T. Gwon, T. Moon, K.D. Kim, and C.S. Hwang. Grain size engineering for ferroelectric hf0.5zr0.5o2 films by an insertion of al2o3 interlayer. *Applied Physics Letters*, 105(19), 2014. ISSN 00036951. URL https://ludwig.lub.lu.se/login?url=https://search.ebscohost.com/login.aspx?direct=true&AuthType=ip,uid&db=edselc&AN=edselc.2-52.0-84910663780&site=eds-live&scope=site.

[23] Hyoungsub Kim, Paul C. McIntyre, and Krishna C. Saraswat. Microstructural evolution of zro2–hfo2 nanolaminate structures grown by atomic layer deposition. *Journal of Materials Research*, 19(2):643 – 650, 2004. ISSN 0884-2914. URL https://ludwig.lub.lu.se/login?url=https://search.ebscohost.com/login.aspx?direct=true&AuthType=ip,uid&db=edssjs&AN=edssjs.F7E80630&site=eds-live&scope=site.

[24] Si Joon Kim, Jaidah Mohan, Scott R. Summerfelt, and Jiyoung Kim. Ferroelectric hf0.5zr0.5o2 thin films: A review of recent advances. *JOM: The Journal of The Minerals, Metals & Materials Society (TMS)*, 71(1):246 – 255, 2019. ISSN 1047-4838. URL https://ludwig.lub.lu.se/login?url=https://search.ebscohost.com/login.aspx?direct=true&AuthType=ip,uid&db=edssjs&AN=edssjs.86A9AAC3&site=eds-live&scope=site.

[25] Burn Jeng Lin. *Optical lithography. here is why.* SPIE, 2021. ISBN 9781510639959. URL https://ludwig.lub.lu.se/login?url=https://search.ebscohost.com/

login.aspx?direct=true&AuthType=ip,uid&db=cat02271a&AN=atoz.
ebs29945311e&site=eds-live&scope=site.

[26] Y.-J. Lin, C.-Y. Teng, Y.-C. Tseng, S.-J. Chang, C. Hu, Y.-F. Liao, and C.-J. Su. Role of electrode-induced oxygen vacancies in regulating polarization wake-up in ferroelectric capacitors. *Applied Surface Science*, 528, 2020. ISSN 01694332. URL `https://ludwig.lub.lu.se/login?url=https://search.ebscohost.com/login. aspx?direct=true&AuthType=ip,uid&db=edselc&AN=edselc.2-52. 0-85086828008&site=eds-live&scope=site.`

[27] D.B. Marshall, M.R. Jarnes, and J.R. Porter. Structural and mechanical property changes in toughened magnesia-partially-stabilized zirconia at low temperatures. *Journal of the American Ceramic Society*, 72(2):218–227 – 227, 1989. ISSN 15512916. URL `https://ludwig.lub.lu.se/login?url=https: //search.ebscohost.com/login.aspx?direct=true&AuthType=ip,uid&db= edselc&AN=edselc.2-52.0-0024612443&site=eds-live&scope=site.`

[28] Park Min Hyuk, Lee Young Hwan, Kim Han Joon, Kim Yu Jin, Moon Taehwan, Kim Keum Do, J. Mu¨ller, A. Kersch, U. Schroeder, T. Mikolajick, and Hwang Cheol Seong. Ferroelectricity and antiferroelectricity of doped thin hfo2-based films. *Advanced Materials*, 27(11):1811 – 1831, 2015. URL `https://ludwig.lub.lu.se/login?url=https: //search.ebscohost.com/login.aspx?direct=true&AuthType=ip,uid&db= inh&AN=15391021&site=eds-live&scope=site.`

[29] J. Müller, T.S. Böscke, D. Bräuhaus, U. Schröder, U. Böttger, J. Sundqvist, P. Kücher, T. Mikolajick, and L. Frey. Ferroelectric zr0.5hf0.5o2 thin films for nonvolatile memory applications. *Applied Physics Letters*, 99(11):112901, 2011. URL `https: //ludwig.lub.lu.se/login?url=https://search.ebscohost.com/login.aspx? direct=true&AuthType=ip,uid&db=inh&AN=12380788&site=eds-live&scope=site.`

[30] Johannes Müller, Tim S. Böscke, Uwe Schröder, Stefan Müller, Dennis Bräuhaus, Ulrich Böttger, Lothar Frey, and Thomas Mikolajick. Ferroelectricity in simple binary zro2 and hfo2. *NANO LETTERS*, 12(8):4318 – 4323, 2012. ISSN 15306984. URL `https://ludwig.lub.lu.se/login?url=https://search.ebscohost.com/ login.aspx?direct=true&AuthType=ip,uid&db=edswsc&AN=000307211000070&site= eds-live&scope=site.`

[31] Takashi Onaya, Toshihide Nabatame, Naomi Sawamoto, Akihiko Ohi, Naoki Ikeda, Takahiro Nagata, and Atsushi Ogura. Ferroelectricity of hfxzr1-xo2 thin films fabricated by 300 °c low temperature process with plasma-enhanced atomic layer deposition. *Microelectronic Engineering*, 215, 2019. ISSN 0167-9317. URL `https://ludwig.lub.lu.se/login?url=https://search.ebscohost. com/login.aspx?direct=true&AuthType=ip,uid&db=edselp&AN= S0167931719301649&site=eds-live&scope=site.`

[32] Anton E.O. Persson, Robin Athle, Pontus Littow, Karl Magnus Persson, Johannes Svensson, Mattias Borg, and Lars Erik Wernersson. Reduced annealing temperature for ferroelectric hzo on inas with enhanced polarization. *Applied Physics Letters NanoLund: Center for Nanoscience*, 116(6), 2020. ISSN 0003-6951. URL `https://ludwig.lub.lu.se/login?url=https://search.ebscohost.com/login. aspx?direct=true&AuthType=ip,uid&db=edsswe&AN=edsswe.oai.lup.lub.lu.se. c3bf612a.365b.49aa.a06d.4d96f07466b8&site=eds-live&scope=site.`

[33] I Petrov, PB Barna, L Hultman, and JE Greene. Microstructural evolution during film growth. *JOURNAL OF VACUUM SCIENCE & TECHNOLOGY A*, 21(5):S117 – S128, 2003. ISSN 07342101. URL `https://ludwig.lub.lu.se/login?url=https://search.ebscohost.com/login.aspx?direct=true&AuthType=ip,uid&db=edswsc&AN=000185671100018&site=eds-live&scope=site`.

[34] S. Riedel, P. Polakowski, and J. Müller. A thermally robust and thickness independent ferroelectric phase in laminated hafnium zirconium oxide. *AIP Advances*, 6(9), 2016. ISSN 21583226. URL `https://ludwig.lub.lu.se/login?url=https://search.ebscohost.com/login.aspx?direct=true&AuthType=ip,uid&db=edselc&AN=edselc.2-52.0-84989895788&site=eds-live&scope=site`.

[35] K. Tomida, K. Kita, and A. Toriumi. Dielectric constant enhancement due to si incorporation into hfo2. *Applied Physics Letters*, 89(14):142902 – 1–3, 2006. URL `https://ludwig.lub.lu.se/login?url=https://search.ebscohost.com/login.aspx?direct=true&AuthType=ip,uid&db=inh&AN=9133757&site=eds-live&scope=site`.

[36] Pierre Villars and Karin Cenzual. Tin crystal structure: Datasheet from "pauling file multinaries edition – 2022" in springermaterials (https://materials.springer.com/isp/crystallographic/docs/sd_1901432). URL `https://materials.springer.com/isp/crystallographic/docs/sd_1901432`. Copyright 2023 Springer-Verlag Berlin Heidelberg & Material Phases Data System (MPDS), Switzerland & National Institute for Materials Science (NIMS), Japan.

[37] Pauli Virtanen, Ralf Gommers, Travis E. Oliphant, Matt Haberland, Tyler Reddy, David Cournapeau, Evgeni Burovski, Pearu Peterson, Warren Weckesser, Jonathan Bright, Stéfan J. van der Walt, Matthew Brett, Joshua Wilson, K. Jarrod Millman, Nikolay Mayorov, Andrew R. J. Nelson, Eric Jones, Robert Kern, Eric Larson, C J Carey, İlhan Polat, Yu Feng, Eric W. Moore, Jake VanderPlas, Denis Laxalde, Josef Perktold, Robert Cimrman, Ian Henriksen, E. A. Quintero, Charles R. Harris, Anne M. Archibald, Antônio H. Ribeiro, Fabian Pedregosa, Paul van Mulbregt, and SciPy 1.0 Contributors. SciPy 1.0: Fundamental Algorithms for Scientific Computing in Python. *Nature Methods*, 17:261–272, 2020. doi: 10.1038/s41592-019-0686-2.

[38] Bert Voigtländer. *Atomic Force Microscopy.* NanoScience and Technology. Springer International Publishing, 2019. ISBN 9783030136536. URL `https://ludwig.lub.lu.se/login?url=https://search.ebscohost.com/login.aspx?direct=true&AuthType=ip,uid&db=cat02271a&AN=atoz.ebs20696059e&site=eds-live&scope=site`.

[39] J. Wang, H.P. Li, and R. Stevens. Hafnia and hafnia-toughened ceramics. *Journal of Materials Science*, 27(20):5397 – 5430, 1992. URL `https://ludwig.lub.lu.se/login?url=https://search.ebscohost.com/login.aspx?direct=true&AuthType=ip,uid&db=inh&AN=4272621&site=eds-live&scope=site`.

[40] J.-H. Yuan, G.-Q. Mao, K.-H. Xue, N. Bai, C. Wang, Y. Cheng, H. Lyu, H. Sun, X. Wang, and X. Miao. Ferroelectricity in hfo2from a coordination number perspective. *Chemistry of Materials*, pages 94 – 103, 2023. URL `https://ludwig.lub.lu.se/login?url=https://search.ebscohost.com/login.aspx?direct=true&AuthType=ip,uid&db=inh&AN=23191274&site=eds-live&scope=site`.